# Experimental analysis on membrane wrinkling under biaxial load - Comparison with bifurcation analysis

Yann Lecieux, Rabah Bouzidi



# Experimental analysis on membrane wrinkling under biaxial load – Comparison with bifurcation analysis

Y. Lecieux, R. Bouzidi

*Nantes University, Institute in Civil and Mechanical Engineering (GeM), UMR 6183, Faculté des Sciences et des Techniques, 2 rue de la Houssinière, Nantes F-44000, France*

This paper presents a detailed experimental study of the formation and evolution of the wrinkle pattern that form in flat elastic and isotropic membranes under the action of in-plane tension. The experiments were carried out on a cruciform specimen stretched along two uncoupled axes using various loading paths. The wrinkled shapes of the membrane were digitized by using a full-field measurement based on the fringe analysis method.

Over this experiment, several phenomena were observed: the mechanism of wrinkle division, the influ-ence of the membrane thickness on the wrinkle pattern, and the reproducibility of a kinematic configuration of wrinkles.

The main result is that non-unique wrinkle shapes have been observed over repeated experiments for nominally identical boundary conditions. The uncertainty of the experimental wrinkle shape has been explained using comparison with the results of a post-buckling finite element analysis.

*Keywords:* Membrane, Gossamer structures, Field measure, Fringe analysis, Bifurcation analysis, Buckling

## 1. Introduction

Over the past 20 years there have been a large number of new structural concepts for large spacecraft applications involving stretched membrane surfaces (Jenkins, 2001). Compared to traditional spacecraft structures, the "Gossamer structures" could provide many advantages such as reduced mass and volume. Gossamer structures are designed for such applications as antennas, solar arrays and telescope lenses. However, the membranes used in gossamer structures cannot undergo compressive stress because of their small bending stiffness. The result of compressive stress is that buckling occurs leading to membrane wrinkling. This may affect the performance and the reliability of the flexible gossamer structures (as in the case of antennas or reflectors). Thus, the prediction of wrinkle patterns in membrane surfaces is one of the many current technological interests in the aerospace industry.

This paper presents a detailed experimental study of the formation and evolution of the wrinkle patterns that form in flat isotropic membranes. The experiments were carried out on cruciform specimens stretched under in-plane uncoupled biaxial loads. The analysis of membrane wrinkling has a long history which started with the works of Wagner (1929). Nevertheless, only recent experimental surveys exist regarding fine details of membrane wrinkling. Indeed, for such compliant material, the measure of the wrinkle shape must be made using a non-contact method. Since the works of Jenkins et al. (1998) several authors have taken interest in the study of wrinkle details and its evolution (Cerda et al., 2002; Wong and Pellegrino, 2006a; Wang et al., 2009). In the present work, results are presented for two uncoupled loading parameters allowing various loading paths while the above mentioned papers deal with the effect of a single loading parameter. The study starts with the presentation of detailed results such as the shape, the amplitude and the wavelength of wrinkles. These data constitute a valuable experimental database for the validation of numerical procedures of wrinkling simulation.

The particular purpose of this work is the observation of the reproducibility of the wrinkle patterns that form on the surface of different specimens for nominally identical boundary conditions. The main result is that non-unique wrinkle shapes have been observed over repeated experiments. These different experimental wrinkle shapes have been reproduced in accordance with the bifurcation theory using a post-buckling finite element analysis.

Experiments performed on a cruciform test specimen are presented in this paper. In each experiment, the whole 3D shape of the membrane has been digitized using a non-contact measurement method: the fringe analysis. The mechanism of wrinkle division has been observed and explained. Wrinkle details for specimens of various thicknesses including the number, amplitude and wavelength of the wrinkles are given here. Then the uncertainty of the wrinkle shape is discussed.

The paper is organized as follows: Section 2 presents a review of previous experimental and numerical works on the topic of thin elastic membrane wrinkling. Section 3 describes the experimental

materials and methods. Experimental results are presented in Section 4 and analyzed in Section 5. In Section 6 the finite element procedure of wrinkling simulation is described and comparison is made between experimental and numerical results. Then Section 7 concludes the paper.

## 2. Review of previous works

### 2.1. Review of experimental measurement of wrinkling

The first survey regarding the wrinkling experiment is attributed to Wagner (1929). He studied the formation of localized buckling in thin metal structures used in the aircraft industry. Later, in the 1960s, NASA developed gossamer structures. The main outcome was the launch of the echo balloon series. At that time, (Stein and Hedgepeth, 1961) offered a theory to analyze partly wrinkled membranes. They carried out an experiment on a flat stretched membrane wrinkled by rotation of a central hub. This study was built upon by the works of Mikulas (1964). More recently, Miyamura (2000) used strain gauges to study the stress distribution in similar structure. He ran experimental results against those obtained through a numerical analysis. Another well-known problem is the shearing of an initially flat rectangular membrane as proposed by Mansfield (1970). He observed the wrinkle orientation on shearing panels in different configurations. However, due to the impossibility of using non-contact methods to measure the out-of-plane displacement, the authors cited above (except for Miyamura on stress measurement) only made qualitative correlations between their experiments and their theoretical results.

Jenkins was the first to provide accurate measurements of wrinkle details. He studied a rectangular panel under shear stress (Jenkins et al., 1998) using a capacitance sensor. Nevertheless, the sensor he used limits the applications to metallic surfaces. Wong and Pellegrino (2006a) carried out two sets of experiments: a rectangular membrane under simple shear, and a square membrane subjected to two pairs of equal and opposite diagonal forces. The measurement of wrinkle details was performed using a laser displacement sensor. This sensor, like the capacitance sensor, does not enable to observe the deflection of the whole membrane, and only cross-sections are measurable.

The use of the photogrammetry method proposed by Blandino enabled the observation of the whole specimen surface. This technique was used to study the effect of symmetric or asymmetric mechanical and thermal loading on membrane wrinkling (Blandino et al., 2001, 2002a,b). The same technique has recently been used by Wang et al. (2009) to study a square membrane in tension. In this experiment, the non-uniform distribution of stress during the application of the tensile loads leads to membrane wrinkling.

### 2.2. Review of numerical procedures of wrinkling simulation

The analysis of the wrinkling behavior of membrane structures started with the works of Wagner (1929), who initiated the method called Iterative Material Procedures (IMP). This method take into account only the in-plane stiffness. The bending stiffness is not evaluated. These wrinkling models are mainly based on the modification of the deformation gradient or of the constitutive equation in order to avoid compressive stresses (Kang and Im, 1997; Epstein and Forcinito, 2001). As a result, this kind of approach does not make it possible to represent wrinkle patterns and does not provide any information about the size of wrinkles. This aspect is a major disadvantage of the membrane model. However, the stress field and wrinkling zone are correctly determined. Mansfield (1968) and Pipkin (1986) reformulated the theory by using a suitable relaxed energy density as defined in the Tension Field Theory. The relaxed energy density represents the average energy per initial area unit over a region containing many wrinkles.

The most adequate method to accurately predict the wrinkle patterns is the use of an extensively refined mesh with thin-shell elements possessing bending stiffness. This approach enables to precisely analyze the buckling and post-buckling response of the membrane under tension. Its detailed developments can be found in Riks (1979) and Crisfield (1997). It involves a geometrical non-linear eigenvalue analysis and leads to the most realistic solution. However, heavy computations are implied due to the dense mesh. A wrinkling analysis, using the buckling of shell element, is typically performed in three stages: The first consists in obtaining a stable initial state in the case of very thin shells. This is often achieved by applying slight initial pre-stress that increased the low bending stiffness of thin shells by the geometrical bending stiffness. The second step is an eigenvalue buckling analysis which gives the mode shapes of the membrane. Mode shapes are introduced as geometrical imperfections in the third step of the post-buckling analysis.

## 3. Experimental program

The aim of this experimental study is to provide a means to characterize the phenomenon of wrinkling for membranes subjected to in-plane loads. The formation and evolution of wrinkles are studied on cruciform specimens. They are tested on biaxial apparatus with various loading paths. The tests are conducted by prescribing displacement in symmetrical way along two orthogonal axes. During the tests, the displacement of each clamped edge as well as the imposed force are measured. To get complete experimental data, the out-of-plane displacement of the tested membrane is also digitized using an optical method of fringe projection.

Additionally, the influence of membrane thickness on wrinkle patterns is considered, as well as the reproducibility of kinematic configurations when several quasi-identical specimens – in terms of material, dimensions and thickness – are submitted to a same given load path. To this end, three identical specimens were tested for each experimental condition. Finally, experiments were performed on nine specimens – with three specimens for each of the three different thicknesses considered.

### 3.1. Biaxial testing apparatus

The biaxial tests were carried out using a particular and dedicated biaxial testing apparatus equipped with two orthogonal, independent, and symmetrical loading axes (see Fig. 1). Along each loading direction, the displacement is applied on the specimen by a pair of cross-bars sliding symmetrically along two parallel guide rails. The displacements of the cross-bars are prescribed manually for each axis thanks to a precision screw, which maintains them at an equal distance from the centre of the device. Each cross-bar is equipped with a displacement probe and a load cell rated 10 kN. Measurement were performed using a displacement sensor with a linearity of 0.2% of full scale and a maximum range of 25 mm.

### 3.2. Specimens

The biaxial tests were performed on cruciform specimens according to the geometry depicted in Fig. 2.

The membrane tested is the Kapton® VN polyimide film, used for spacecraft applications. Table 1 (DuPont, 2006) summarizes the material characteristics of the specimens.

### 3.3. Test procedure

The steps of the experimental protocol performed on the specimens presented in Table 1 include the positioning of the

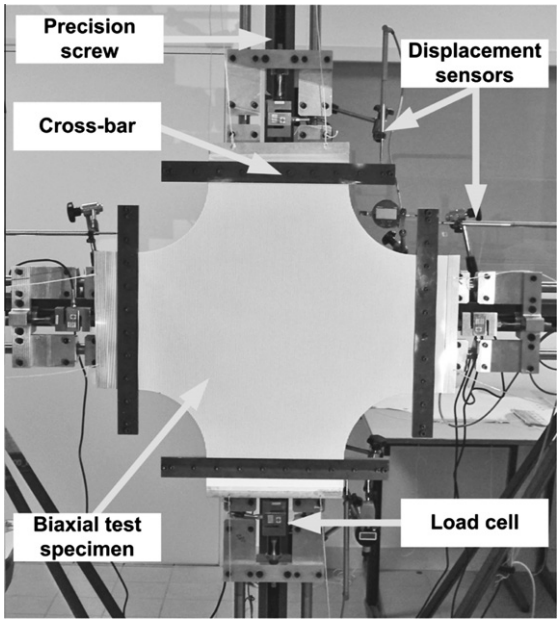


**Fig. 1.** Biaxial testing machine.

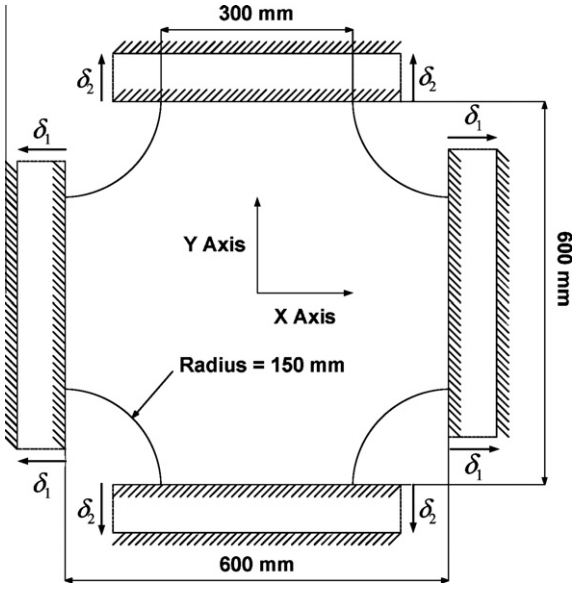


**Fig. 2.** Geometry of the tested specimens.

**Table 1**
Material characteristics of tested membranes.

| Thickness (μm) | Number of test specimens | Type of Kapton | Young modulus (MPa) | Poisson ratio |
|---|---|---|---|---|
| 125 | 3 | VN | 2800 | 0.34 |
| 50 | 3 | VN | 2800 | 0.34 |
| 25 | 3 | VN | 2800 | 0.34 |

membrane on the apparatus, then the application of a small initial stress to its four edges before clamping the membrane to the four cross-bars. Finally, the desired displacement paths are applied.

During membrane installation, the biaxial testing machine is placed in horizontal position. A slight initial tension is applied to the membrane by means of counterweight connected through cords running over pulleys via aluminum rigid blocks glued to the four edges of the specimen. A similar system was used in the study of Wong and Pellegrino (2006a). The total value of the counterweight applied on one edge is given in Table 2.

These preloading values guarantee identical stress field for the three thicknesses and hence a quasi plane shape for the membrane. The membrane is then clamped to the cross-bars. The different elements described above are shown in Fig. 3.

After clamping the specimen, various displacement paths are applied to the cross-bars. Table 3 summarizes the applied paths (with $i = 1 \rightarrow 7$).

For each prescribed displacement, the acquired data are the in-plane displacements, the loads applied on the edges of the specimen, and also the out-of-plane displacements of the membrane caused by the wrinkling phenomenon.

### *3.4. Measure of the out-of-plane displacement*

To measure the shape of the wrinkles, the technique called "Fringe projection method" was used, see Robinson and Reid (1993) and Yoshizawa (2009). It is based on the analysis of the deformation of fringes projected onto the studied object, which acts as a screen. The fringes are projected thanks to a standard video projector. It is a full-field and non-contact method which provides the deflection $z$ of every point of the deformed surface. During the test, images of cruciform specimens are recorded for each loading step using a CCD camera. For each displacement step, this method allowed the digitization of the 3D shape of the whole membrane.

**Table 2**
Preloading counterweight values.

| Thickness (μm) | Total value of counterweight (g) |
|---|---|
| 125 | 1000 |
| 50 | 400 |
| 25 | 200 |

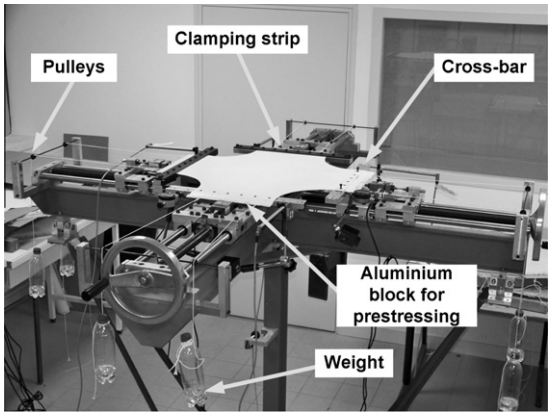


**Fig. 3.** Positioning of the membrane.

**Table 3**
Prescribed displacement paths.

| Load path $i$ | |
|---|---|
| $\delta_1$ (mm) | $\delta_2$ (mm) |
| $-[0.5 \times (i-1)]$ | 0 |
| $-[0.5 \times (i-1)]$ | 0.5 |
| $-[0.5 \times (i-1)]$ | 1.0 |
| $-[0.5 \times (i-1)]$ | 1.5 |
| $-[0.5 \times (i-1)]$ | 2.0 |
| $-[0.5 \times (i-1)]$ | 2.5 |
| $-[0.5 \times (i-1)]$ | 3.0 |

### 3.5. Fringe deformation method

To measure the wrinkling induced membrane deflection, two pictures of the projected pattern are taken: one of the initial configuration corresponding to the reference plane, and the other of the deformed wrinkled shape. The deformation of the fringe pattern between these two configurations is directly related to the deflection.

A pattern of vertical fringes is projected obliquely onto the membrane with an angle $\theta$, using a video projector. The intensity of the light signal recorded on the membrane can be expressed as:

$$I(x,y) = I_0(x,y)\left[1 + \gamma(x,y)\cos\left(\frac{2\pi x}{p}\right)\right] \quad (1)$$

where $I_0(x,y)$ is the average intensity (or bias) of the signal, $\gamma(x,y)$ is the contrast, and $p$ is the fringe width. In (1), it is assumed that the projected fringes are parallel to the $y$ axis.

When wrinkles appear over the stretched membrane, it is no longer plane. Since the deformed shape acts as a screen, the projected patterns of parallel fringes undergo a displacement which depends on the height $z$, and on the angle of projection $\theta$ (see Fig. 4).

$$u_x = z(x,y)\tan\theta \quad (2)$$

The deformation of the fringes leads to a variation of the fringe width $p$ on the recorded picture. The shift of the fringes in the direction $x$ can be viewed as a phase of the light signal $\varphi(x,y)$. The light intensity of deformed patterns can also be written as (Surrel and Surrel, 1998):

$$I(x,y) = I_0(x,y)\left[1 + \gamma(x,y)\cos\left(\frac{2\pi x}{p} + \varphi(x,y)\right)\right] \quad (3)$$

where

$$\varphi(x,y) = \frac{2\pi\tan\theta}{p} z(x,y) \quad (4)$$

The phase map $\varphi(x,y)$ of the pictures was obtained thanks to a Fourier transform and inverse Fourier transform of the recorded pictures Holo3 (2006).The commercial software Fringe Analysis® was used in this study.

The notation $\varphi(x,y)$ designated the phase map observed on the wrinkled membrane and $\varphi_0(x,y)$ the phase map of the plane membrane. The difference between the two can be noted:

$$\Delta\varphi(x,y) = \varphi(x,y) - \varphi_0(x,y) = \frac{2\pi x}{p} z(x,y)\tan\theta \quad (5)$$

Since the phase variation $\Delta\varphi(x,y)$ is computed modulo $2\pi$, it is necessary to unwrap it. The different steps of the method are summarized in Fig. 5.

The parameter $\theta$ is needed to convert the unwrapped phase into amplitude (see (5)). However, it is difficult to evaluate $\theta$ with accuracy. Rather than measuring the angle $\theta$, it was decided to calibrate the system. The most used calibration method is presented by Zhang et al. (2004). It consists in incrementally modifying the distance of the CDD camera to the reference plane, in order to adjust the linear coefficient linking phase and deflection $z(x,y)$. In this study, the calibration was achieved using two gauge blocks of different heights placed on the reference plane of the testing device. Measuring their heights enables the identification of the parameter $\theta$.

### 3.6. Estimation of the resolution $\Delta z$ of the optical measure

The resolution $\Delta z$ of the optical measure is defined as follows, see Surrel and Surrel (1998):

$$\Delta z = \frac{L}{RN\tan(\theta)} \quad (6)$$

where $L$ is the length of the measured specimen in the $x$ direction (assumed orthogonal to the fringe direction), $N$ is the number of fringes, and $R$ is the phase resolution – the number of grey levels readable by the fringe analysis software. For the experimental parameters described in Table 4, the resolution of the optical method is around 25 μm.

One advantage of the fringe projection method is the possibility to set the resolution $\Delta z$. Indeed if an enhanced resolution is required, several solutions are available:

- Increasing the projection angle $\theta$.
- Focusing on a smaller observed area.
- Increasing the number of projected fringes.

However, the angle $\theta$ cannot be increased to higher values (close to $\frac{\pi}{2}$). This would lead to the formation of shadow areas. The number of fringes $N$ has to be set to have at least four pixels per fringe which is the value proposed in Surrel and Surrel

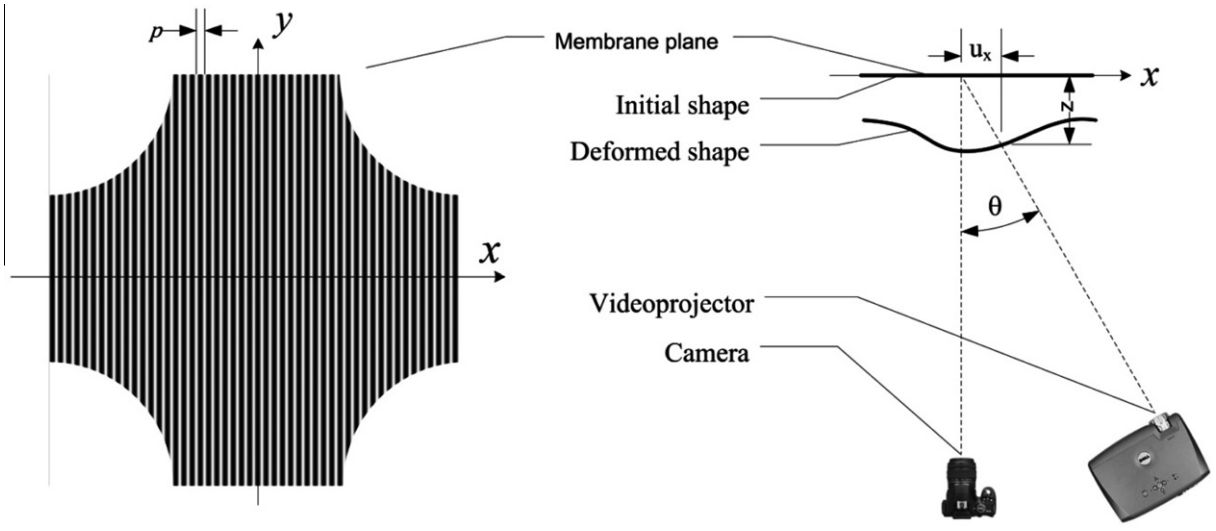


**Fig. 4.** Optical measure principle.

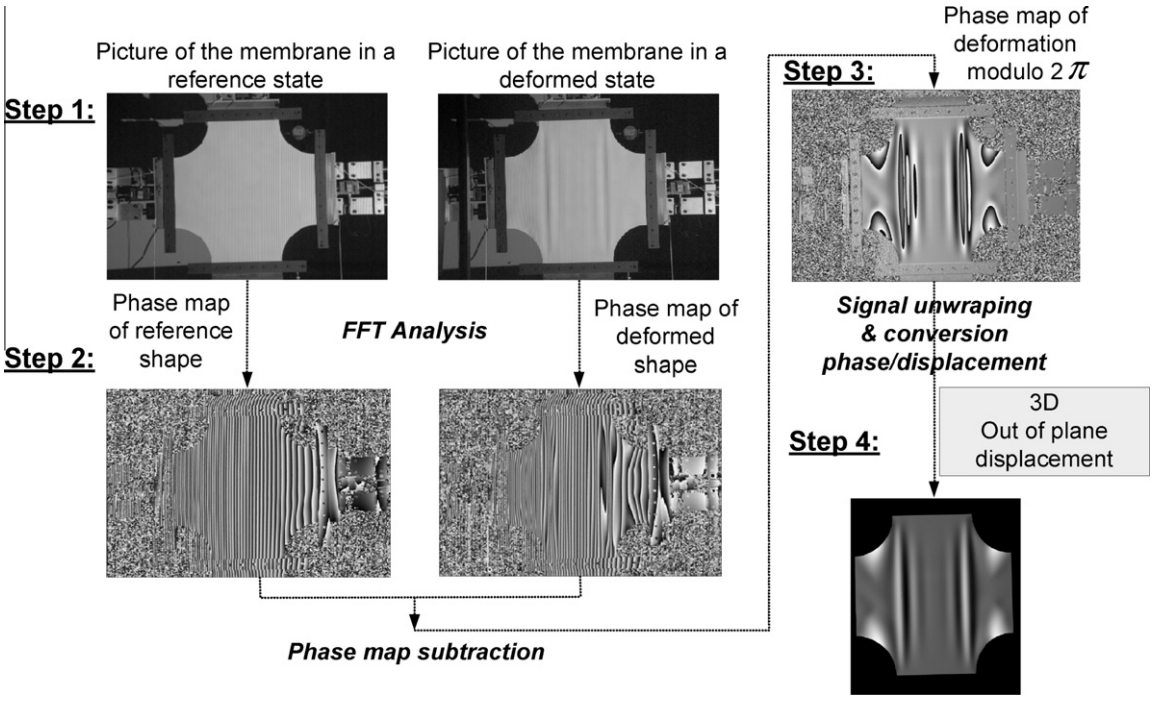


**Fig. 5.** Principle of picture analysis as used in the fringe projection method.

**Table 4**
Experimental parameters for the optical measure.

| | |
|---|---|
| Angle of projection $\theta$(deg) | 40 |
| Number of pixels | 4500 × 3000 |
| Number of fringes $N$ | 280 |
| Phase resolution $R$ | 100 |
| Length of observed shape $L$ (mm) | 600 |

(1998). In this experiment, the number of pixels is about 12 per fringe.

## 4. Experimental results

This section presents detailed experimental results on the evolution of the shape of wrinkles under load. In particular, the mechanism of wrinkle division is explained. Then, the reproducibility of the kinematic configurations of the wrinkles is discussed.

### 4.1. Wrinkle patterns

The typical wrinkle pattern of a deformed membrane (see Fig. 6) shows a double symmetric shape with three main regions of instability. There are slack zones near the circular edges of the membrane. In the middle area, the presence of primary wrinkles parallel to the direction of the tension loading, axis $y$ is visible. Finally, there are transition zones between the primary wrinkles and the slack zones. These are called secondary wrinkling zones by analogy with the work of Wang et al. (2009).

The wrinkle represented in the above pattern is generic. More specifically, the presence of slack zones and secondary wrinkles depends on the loading path. Photographic samples of the membrane shape for different prescribed displacements are shown in Fig. 7.

This pictorial matrix shows widely varying geometrical configurations of wrinkles. This is due to the control of the applied displacement with two independent parameters. Here, the seven

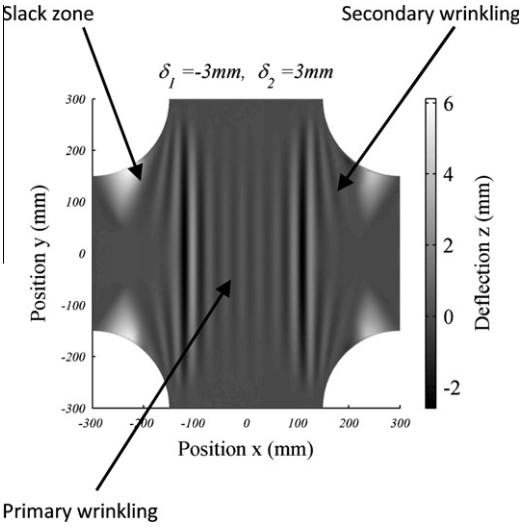


**Fig. 6.** Sample of experimental out-of-plane displacements (specimen thickness = 50 μm).

loading paths studied for each of the nine test specimens formed a really consequent experimental database. Indeed, each loading path constitutes a possible validation case for numerical procedures of wrinkling simulation.

### 4.2. Modification of shape under load

Wrinkle details and their formation mechanisms are further investigated by plotting three cross-sections of the tested specimens, in particular by plotting the out-of-plane displacement $z$ against the $x$ axis at different values of $y$. Fig. 8b and c shows samples of the obtained cross-sections for a given load step ($\delta_1 = -0.5$ mm and $\delta_2 = 3$ mm). The central section, ($y = 0$), gives useful characteristics of primary wrinkling while sections at

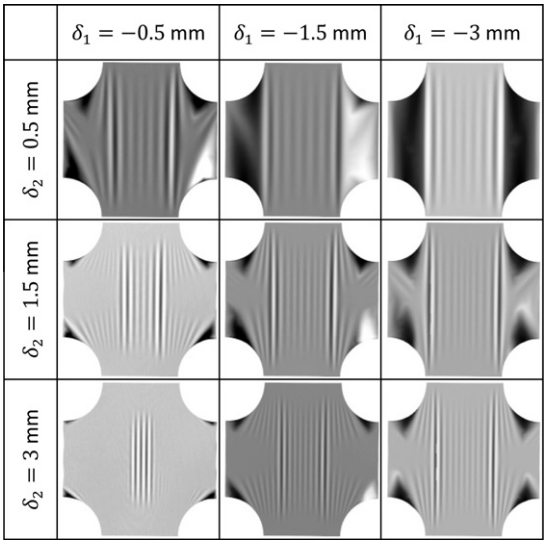


**Fig. 7.** Pictorial matrix representation of deformations obtained on tests performed on a 25 μm membranes.

$y = \pm 150$ mm give information about the primary wrinkling, the secondary wrinkling and the slack zone.

Thanks to the experiment, different mechanisms of the formation and disappearance of wrinkles have been shown. First, for a given compressive displacement ($\delta_1$), it was observed that when the tensile displacement ($\delta_2$) increases gradually, a new wrinkle is suddenly created by division of an existing wrinkle. An experimental sample of wrinkle creation by division is given in Fig. 12. This sudden change in the number of wrinkles, called "mode jumping", was already encountered in plate buckling situations, see Stein (1959). In the particular case of membrane wrinkling, the phenomenon was observed by Wong and Pellegrino (2006a).

Furthermore, the creation of secondary wrinkles in the initially slack zones was noticed. These secondary wrinkles could in certain cases join to lead to the creation of primary wrinkles. The same evolution mechanism of secondary wrinkles was depicted in Wang et al. (2009).

Nevertheless, the main mechanism leading to the creation of primary wrinkles is the sudden division of an existing wrinkle when the tensile displacement, and therefore the tensile load, increase.

### 4.3. Wrinkles subdivision

The mechanism of wrinkle subdivision is the result of bifurcation from an equilibrium situation of two opposite forces.

A wrinkle can be represented as a surface with double curvature. The eigen curvature directions coincide with the longitudinal direction (stretched) and the transversal direction (compressed). Along the longitudinal direction, the tension stress tends to push back the peak of the wrinkle down to the median plane (see Fig. 9). Whereas, in the transversal direction, the compressive stress tends to bend the membrane and therefore prevents it from

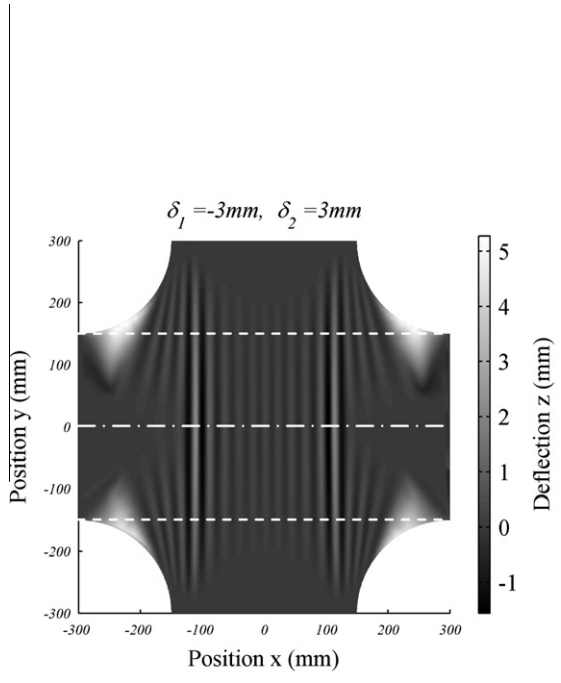


(a) Experimental out of plane displacement

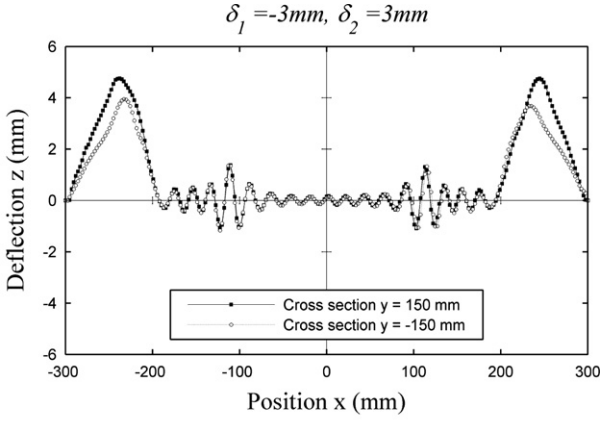


(b) Cross section at y=+/-150 mm

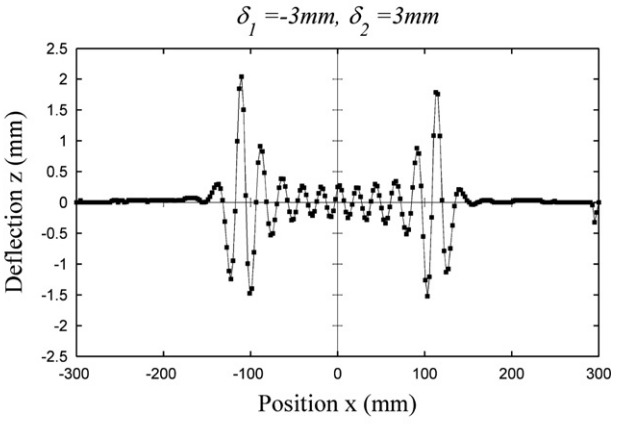


(c) Central cross section at y= 0 mm

**Fig. 8.** Sample of experimental data processing (specimen thickness = 25 μm).

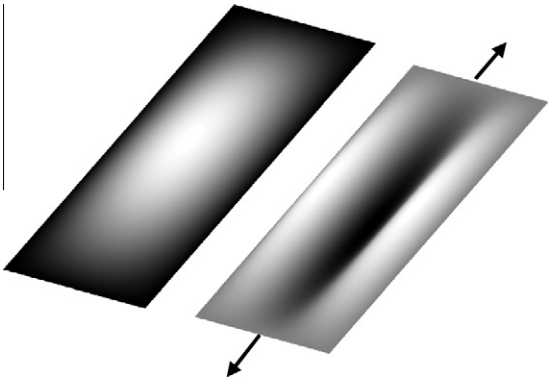

**Fig. 9.** Wrinkle shape during subdivision.

returning to the median plane. A thin strip of the wrinkle with its applied stresses has been sketched in Fig. 10.

This equilibrium is maintained as long as the critical buckling value is not reached. By increasing the tension in the longitudinal direction, the amplitude of the wrinkles increases under Poisson's effect. When the critical amplitude is reached, the wrinkle collapses and leads to new shapes with one peak and one trough in case of asymmetrical bifurcation or two peaks and one trough in case of symmetrical bifurcation, as shown in Fig. 11.

In order to focus on the mechanism of wrinkle subdivision itself, a dedicated measurement has been performed on a test specimen of 125 μm. The measurement of the wrinkle shape has been performed just before and after a wrinkle collapsed. Fig. 12a shows the division of the central wrinkle for $\delta_2 = 0.08$ mm which collapses when increasing the tensile displacement $\delta_2 = 0.08$ mm to $\delta_2 = 0.09$ mm.

The superimposition of the two shapes just before and after the central wrinkle collapses shows clearly that only the shape of the central wrinkle changes between the two configurations. Here the creation of the new wrinkle can be explained as a local mode change, or a local buckling of the existing wrinkle. Then, when further increasing the tensile displacement up to $\delta_2 = 0.15$ mm, Fig. 12b shows the evolution of the wrinkle shape in terms of amplitude and spatial distribution after the creation of the new wrinkle. Nevertheless, until an existing wrinkle collapses, this evolution of wrinkle pattern is made without change in the number of wrinkles.

### 4.4. Reproducibility of wrinkle pattern

By applying quasi-identical experimental conditions three times for three distinct specimens, the aim was to verify the reproducibility of a wrinkle pattern. The experimental observations

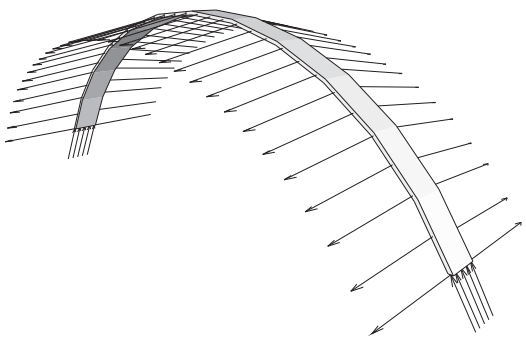

**Fig. 10.** Wrinkle strip and its stress loading.

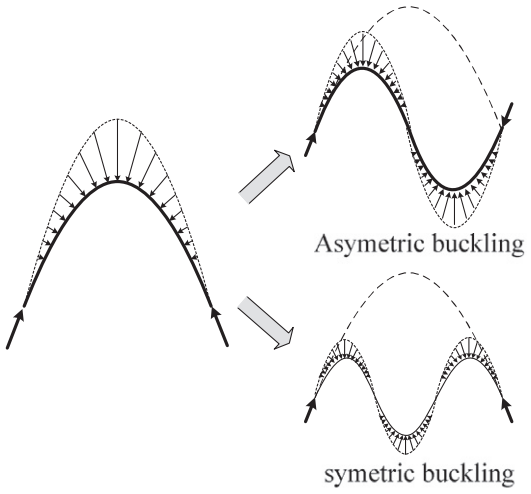


**Fig. 11.** Buckling of an existing wrinkle.

showed that very close experimental conditions (membrane thickness, geometry and loading case) could lead to different wrinkle patterns. Fig. 13 shows the cross-section of two membranes of Kapton 50 μm when the displacements $\delta_1 = -3$ mm and $\delta_2 = 1$ mm has been applied. For test specimen 1, the wrinkle pattern is symmetric, whereas for test specimen 2, the wrinkle pattern is asymmetric. The number of primary wrinkles is also different. More precisely, if each local extremum is counted as a wrinkle (except local maximum near the edge for test specimen 1) there are 17 wrinkles for test specimen 1 and only 16 for test specimen 2.

Wong and Pellegrino (2006a), as well as Balmforth et al. (2008), have already observed different wrinkle patterns on membranes subjected to shear loading, uploading and reloading cycles. These observations could be explained by hysteresis loops resulting on the one hand from unloading on an unstable equilibrium branch and, on the other hand, from the yielding of the material during the first loading cycle, as explained in Wong and Pellegrino (2006a).

In the case of this study, the uncertainty on the wrinkled shape is due to very small perturbations of the experimental conditions, such as the initial shape and boundary conditions. To confirm this assertion, the initial bifurcation mode, which appears when performing the negative displacement $\delta_1$, has been noted down. Two different modes were observed with symmetric and asymmetric shapes. Samples of both symmetric and asymmetric patterns observed during the experiment are shown in Fig. 14. Table 5 summarizes the kind of initial bifurcation modes that were observed for each of the three 125 μm thick specimens. Similar results are presented in Table 6 for the 50 μm thick specimens. However, for this thickness, the initial bifurcation mode is observed for a tensile displacement $\delta_2 = 0.5$ mm. This allowed to stabilize the shape of the membrane which is quite chaotic for $\delta_2 = 0$ mm, due to the very small thickness of the specimen.

Table 5 shows that the asymmetric shape was observed more often than the symmetric one – fifteen times for asymmetric one against three times for symmetric. This asymmetric shape corresponds to the first buckling mode of the structure, as explained in Section 6. For the 50 μm thick specimen, Table 6 shows that the asymmetric mode was observed twelve times against six times for the symmetric one. It appears that the uncertainty in the wrinkle configuration rises as the specimen thickness decreases.

Nevertheless, the wrinkle configuration of one test specimen is not only driven by its initial configuration. Indeed, when performing similar load paths on two specimens with initially quasi-similar wrinkle shape, the final wrinkle patterns can be different.

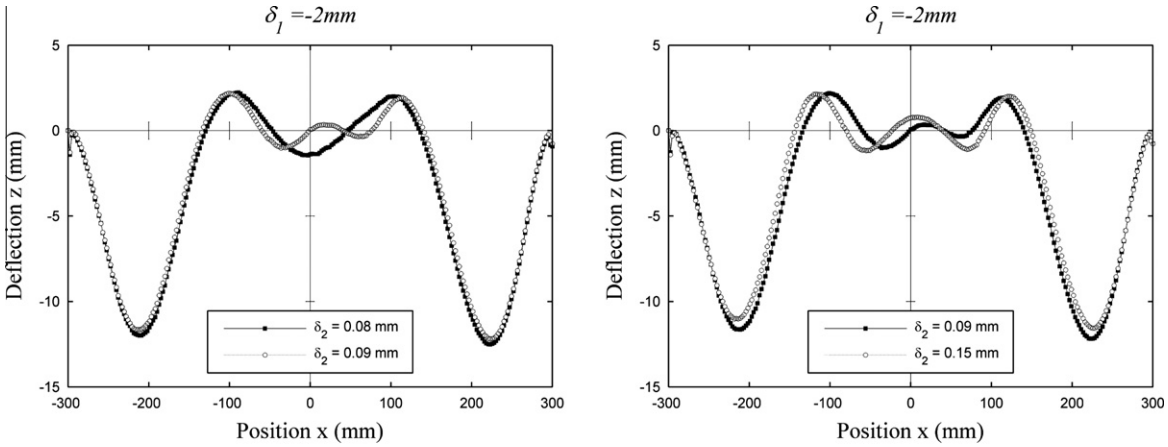


*(a) Central cross section just before and after the central wrinkle collapses*

*(b) Evolution of the wrinkle shape after the central wrinkle collapses*

**Fig. 12.** Mechanism of wrinkle creation by division (specimen thickness = 125 μm).

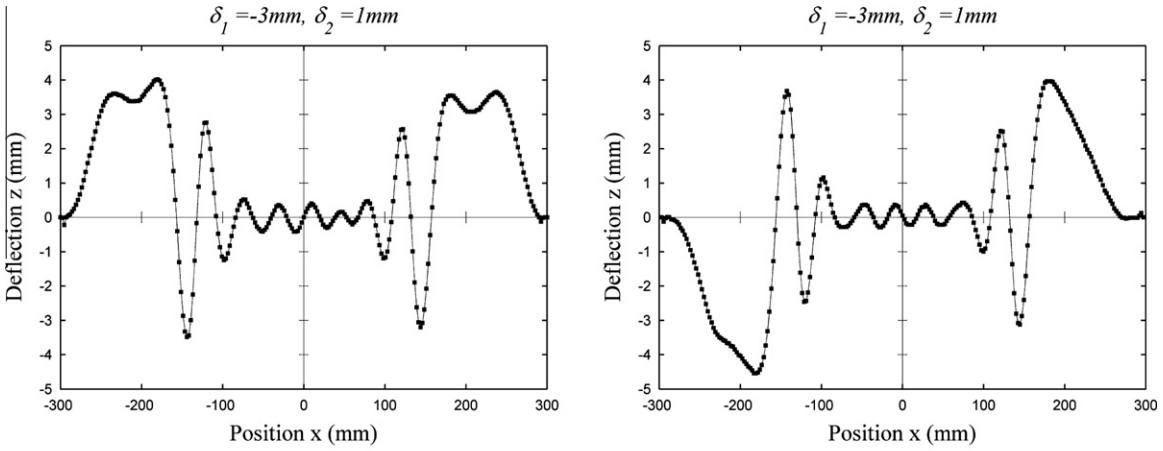


Central cross section of the 50 μm test specimen n°1
Symmetric pattern

Central cross section of the 50 μm test specimen n°2
Asymmetric pattern

**Fig. 13.** Comparison between two wrinkle patterns for identical load cases.

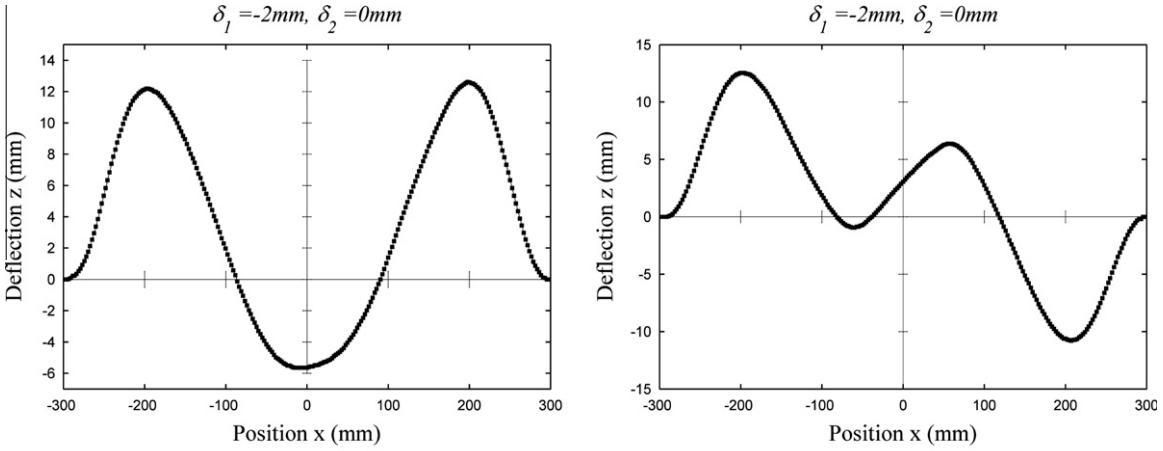


(a) Initial symmetric mode
Specimen 1

(b) Initial asymmetric mode
Specimen 2

**Fig. 14.** The two initial wrinkle shape configurations (specimen thickness = 125 μm).

**Table 5**
Geometry of the initial bifurcation mode (specimen thickness 125 μm).

| Load path *i* | Specimen 1 | Specimen 2 | Specimen 3 |
|---|---|---|---|
| 2 | Symmetric | Asymmetric | Asymmetric |
| 3 | Asymmetric | Asymmetric | Symmetric |
| 4 | Asymmetric | Asymmetric | Asymmetric |
| 5 | Symmetric | Asymmetric | Asymmetric |
| 6 | Asymmetric | Asymmetric | Asymmetric |
| 7 | Asymmetric | Asymmetric | Asymmetric |

**Table 6**
Geometry of the initial bifurcation mode (specimen thickness 50 μm).

| Load path *i* | Specimen 1 | Specimen 2 | Specimen 3 |
|---|---|---|---|
| 2 | Asymmetric | Asymmetric | Symmetric |
| 3 | Symmetric | Symmetric | Asymmetric |
| 4 | Asymmetric | Asymmetric | Asymmetric |
| 5 | Asymmetric | Asymmetric | Asymmetric |
| 6 | Symmetric | Asymmetric | Symmetric |
| 7 | Symmetric | Asymmetric | Asymmetric |

Diverse bifurcation modes can occur for nominally similar experimental conditions when performing the tensile displacement $\delta_2$. A sample is given in Fig. 15. Here the two specimens present a quasi-similar wrinkle pattern for $\delta_1 = -2.5$ mm and $\delta_2 = 0.5$ mm. Then for $\delta_1 = -2.5$ mm and $\delta_2 = 3$ mm, the wrinkle pattern of specimen 1 presents one more wrinkle than in specimen 2.

Wrinkling strongly depends on test conditions. Very small perturbations of the experimental conditions can affect the resulting wrinkle pattern. Speaking about one shape (in terms of wrinkle pattern) for a given load case is practically meaningless, especially for very thin membranes. The prediction of the particular shape that would occur for a given load case seems uncertain.

## 5. Wrinkle shape analysis

The sensitivity of the shape of the wrinkles with respect to the experimental conditions makes it necessary to define common properties of the wrinkle patterns. The number, wavelength and amplitude of wrinkles are presented as function of loading conditions. These synthetic results can be used as comparative reference for numerical models. In this way, it is proposed to use the envelope curve of the wrinkles. Then, the influence of the thickness of the specimens on the elements described above is discussed.

### 5.1. The envelope curve of the wrinkles

To avoid considering the fluctuations of the wrinkle patterns with respect to the experimental conditions, envelope curves were used to represent the wrinkle shapes.

The following explains how to obtain it. First, it was assumed that the sign (positive or negative) of the out-of-plane displacement is totally unpredictable and has no impact on the wrinkle pattern properties. So only the absolute value of $z$ is considered. Then, the local maximums corresponding to the crest of each wrinkle are identified. Finally, the envelope curve of a given cross-section is plotted by linking up its local maximums.

To avoid the wrinkles of the slack zones for which the shape is somewhat chaotic, the area of interest is limited to the central zone ($-150$ mm $\leqslant x \leqslant 150$ mm). Fig. 16 shows how the profile in Fig. 16a is processed in Fig. 16b.

Envelope curves for a given load case are compared by superimposing the nine curves on the same graph. Samples of experimental envelope curves are shown in Figs. 17 and 18.

The envelope curves obtained for three test specimens of a given thickness are very close to each other. This allows to make comparisons between a single kinematic configuration obtained by simulation and those observed experimentally. Furthermore, noticeable differences are observed between envelope curves of different thicknesses. Figs. 17 and 18 show that the amplitude of the envelope curve of the wrinkles decreases along with the thickness of the membrane.

### 5.2. Evolution of wrinkle properties

To investigate the evolutions of the wrinkle properties, the evolution of the number, the amplitude and the wavelength of wrinkles have been plotted for a given thickness. The response surfaces are presented in Fig. 19 for the 125 μm specimens, in Fig. 20 for those of 50 μm and in Fig. 21 for the 25 μm specimens.

The results presented in these graphs for a given thickness are the averages of the values obtained for the three specimens of a given thickness. To find out the number of wrinkles, each local maximum of the absolute value of $z$ in the area ($-150$ mm $\leqslant x \leqslant 150$ mm) is here counted as a wrinkle. The half-wavelength thus correspond to the distance between two local maximums on this curve, and the amplitude maximum is the maximum of the local maximums.

For similar reasons as the envelope curves, the area of interest is limited to the central zone ($-150$ mm $\leqslant x \leqslant 150$ mm).

It can be noticed that the maximal amplitude of wrinkles and their wavelength decreased when increasing the tensile displace-

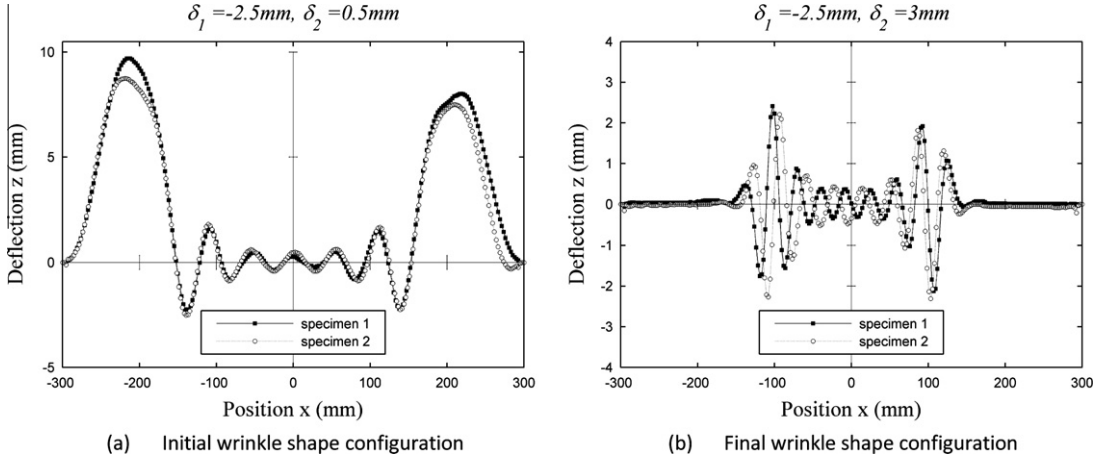


**Fig. 15.** Evolution of two initially identical wrinkle shapes (specimen thickness = 50 μm).

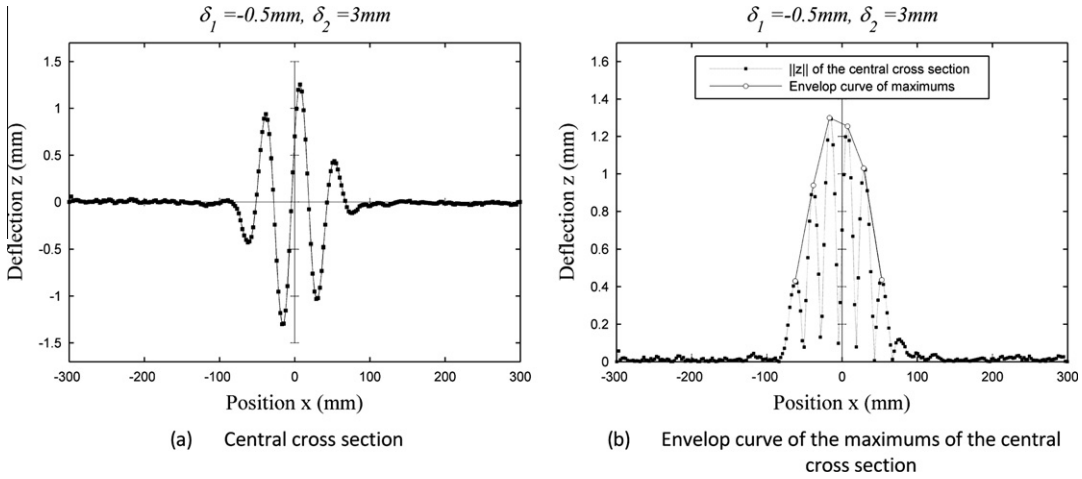


**Fig. 16.** Sample of envelope curve of the maximum of the central cross-section (specimen thickness = 125 μm).

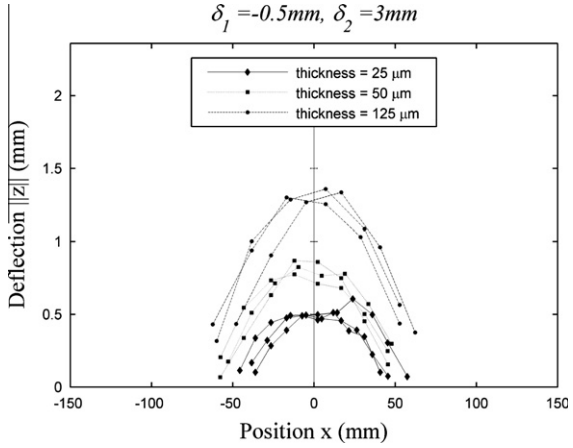


**Fig. 17.** Experimental envelope curves obtained for $\delta_1 = -0.5$ mm and $\delta_2 = 3$ mm.

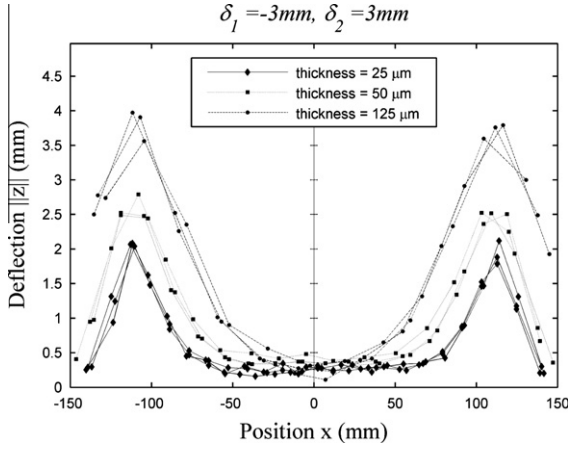


**Fig. 18.** Experimental envelope curves obtained for $\delta_1 = -3$ mm and $\delta_2 = 3$ mm.

ment $\delta_2$. Nevertheless, the same conclusion cannot be drawn regarding the evolution of the number of wrinkles. The load path $\delta_1 = -0.5$ mm clearly shows that the number of wrinkles reaches a maximum before decreasing with an increasing $\delta_1$.

At the beginning of the tensile displacement application, the shape is characterized by the presence of a single wrinkle. This wrinkle has an important amplitude and wavelength. When the tensile load is gradually increased, new wrinkles are created by division of existing ones. A diminution of the wavelength was thus experimentally observed. Furthermore, the amplitudes of the wrinkles tend to equalize, and hence the maximum amplitude of wrinkles to decrease.

To explain the evolution of the number of wrinkles, the particular geometry of the test specimens has to be considered. Indeed, due to the geometry, the area where the compressive stress is applied decreased as the tensile load increased. Thus, at first, the creation of wrinkles by division was observed, and then, the existing wrinkles closed up to the center of the membrane. Furthermore, the slack zones, secondary and the primary wrinkles near the cross-bars can possibly completely disappear (see Fig. 7 $\delta_1 = -0.5$ mm and $\delta_2 = 3$ mm).

### 5.3. Influence of membrane thickness

The study of the influence of thickness on geometrical properties of the wrinkle patterns is carried out by superimposing on the same graph the data issued from the three thicknesses tested during the experiment. The evolution of the wrinkle properties (i.e. wavelength, amplitude and number of wrinkles) were plotted when the tensile displacement $\delta_2$ increased for a fixed $\delta_1$.

A sample is given here in Figs. 22–24 for $\delta_1 = -3$ mm.

The figure presented here shows that the number of wrinkles increases when then thickness of the membrane decreases. Furthermore, the average wavelength and the maximal amplitude follow the same evolution. The last two observations were already made by Wong and Pellegrino (2006a) in the study of a membrane under corner loads.

Bending energy is proportional to thickness. It is thus more convenient for a thin structure than for a thick one to form many wrinkles. This observation shows that when the thickness decreases, the behavior of a thin structure comes very close to the behavior of a "true membrane". Nevertheless, "true membranes" do not have physical reality in this study because a small bending rigidity always exist.

In many approaches related to wrinkling analysis, the thickness of the membrane is not taken into account. Even though the bending stiffness is very small in thin shells, it is fundamental in wrinkling deformation since, after buckling, it highly influences the shape of the wrinkle. Indeed, the bending stiffness, even if very low, is the parameter which, in conjunction with in-plane tension, determines the shape of the wrinkles in terms of amplitude and wavelength.

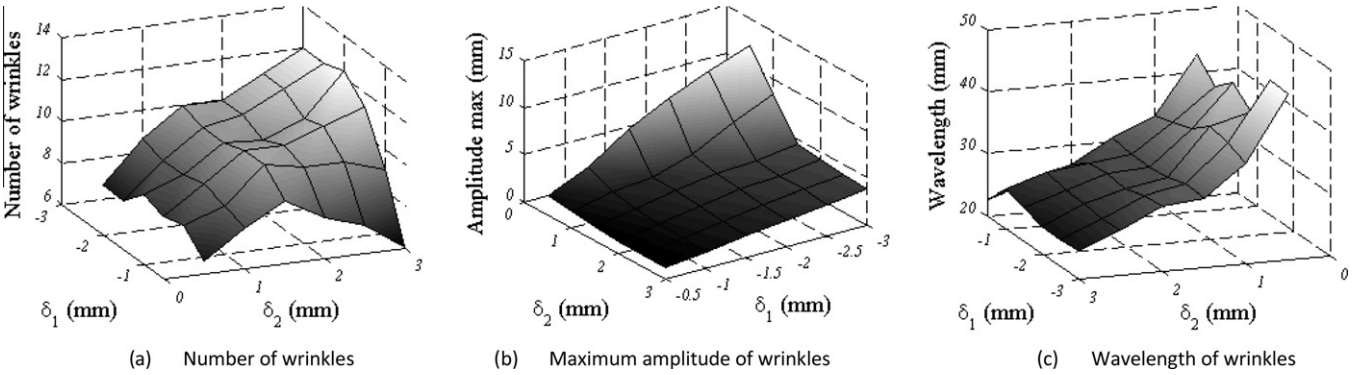


**Fig. 19.** Overview of experimental results concerning the 125 μm specimens.

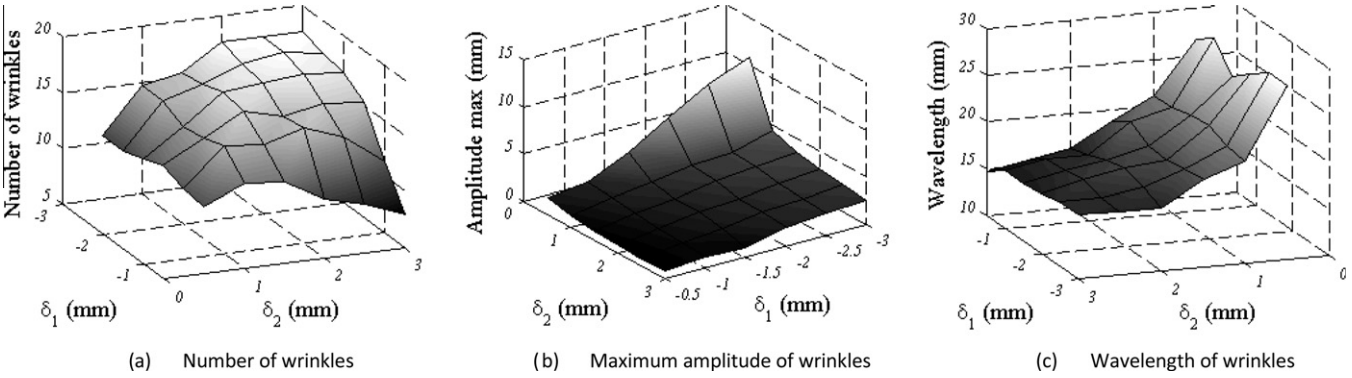


**Fig. 20.** Overview of experimental results concerning the 50 μm specimens.

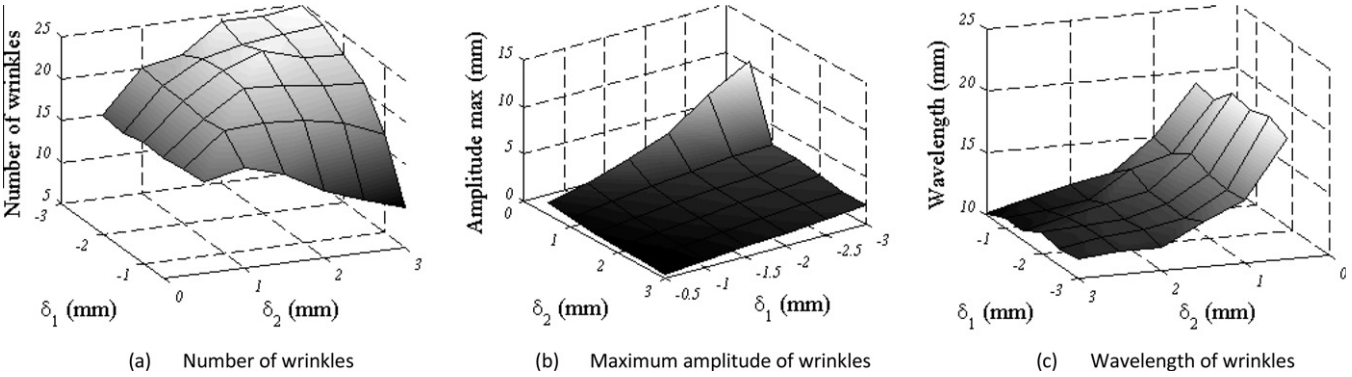


**Fig. 21.** Overview of experimental results concerning the 25 μm specimens.

## 6. Bifurcation analysis of wrinkling

This section aims at providing an explanation to the non-reproducibility of the wrinkle patterns observed experimentally when several quasi-identical specimens – in terms of material, dimensions and thickness – are submitted to a same given load path. Results presented here showed that the different kinematic configurations obtained during the experiment could be numerically reproduced in accordance with bifurcation theory. The procedure of wrinkling simulation was performed using a post-buckling analysis. The model used in this study was proposed by Wong and Pellegrino (2006b).

### *6.1. Numerical model*

The shell element S4R (code ABAQUS®) was used to investigate the wrinkling simulation. Such a shell element has a reduced integration with four nodes and six freedoms per nodes. A structured mesh of 16,000 elements with a uniform element size in the central area (2.5 mm) was used to model the whole structure. The size of the mesh element is chosen to have enough elements per wrinkle to capture the wrinkle details. The mesh used during the analysis is shown in Fig. 25.

The four edges of the membrane are assumed to be fully constrained on the cross-bars. A uniform displacement $\delta_1$ is prescribed on the vertical edges along the $x$-axis, and then a uniform displacement $\delta_2$ is imposed on the horizontal edges along the $y$-axis (see Fig. 2).

First, the experimental Young's modulus and the Poisson's ratio corresponding to our experimental conditions (the global strain imposed upon the structure is less than 1%) have been identified. Indeed the behavior of the Kapton® is relatively non-linear and different Young's moduli and Poisson's ratios are given in the bibliography. The identification of the Young's modulus and the Poisson's

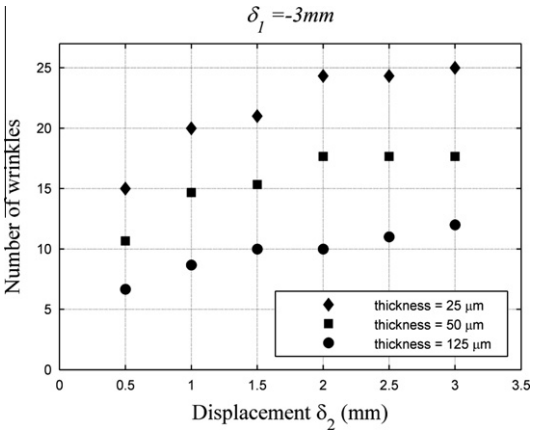


**Fig. 22.** Average number of wrinkles in the central cross-section in membranes of different thicknesses.

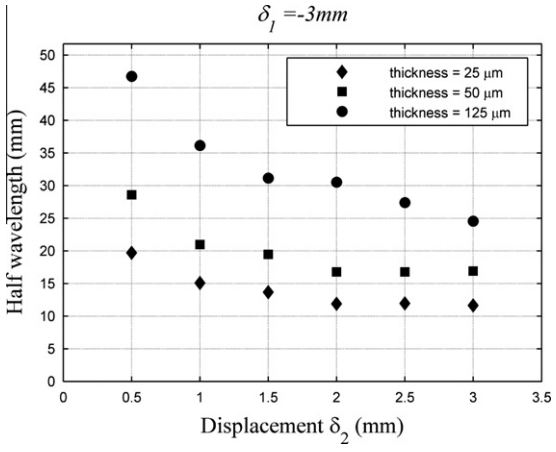


**Fig. 23.** Average of wrinkle wavelengths in the central cross-section in membranes of different thicknesses.

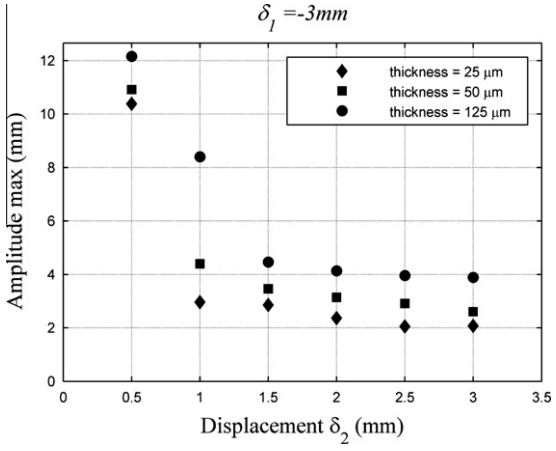


**Fig. 24.** Average of maximum amplitude of wrinkles in the central cross-section in membranes of different thicknesses.

ratio is carried out using the experimental results of load path 1 ($\delta_1$ = 0 mm and $\delta_2$ = 0–3 mm) i.e. without wrinkles occurring during the loading. The inverse analysis is done by fitting the loads obtained by simulation to the experimental loads recorded on the two axes. The most appropriate parameters are $E$ = 3350 Mpa and $v$ = 0.3.

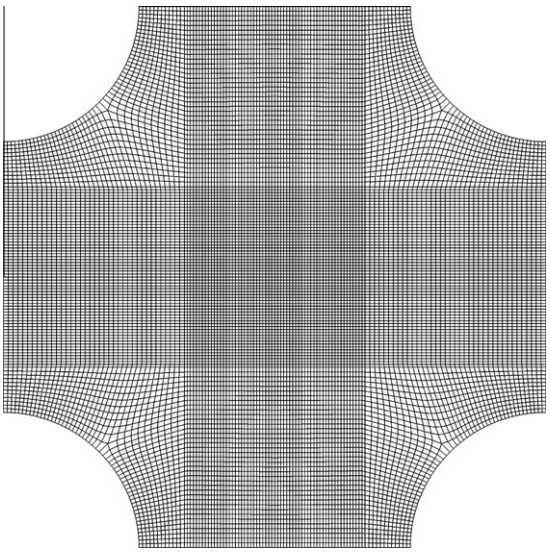

**Fig. 25.** Finite element model.

These parameters have then been used in the post-buckling analysis to predict the wrinkle patterns. The loads recorded during the experiment for the whole experiment are given in Table A.7. These data are used as validation data and compared with those predicted through the numerical analysis.

### 6.2. Wrinkle simulation procedure

The numerical procedure of wrinkling simulation used in this study was presented in (Wong and Pellegrino, 2006b) using the software ABAQUS®. An eigenvalue buckling analysis is carried out using the Lanczos method to obtain the possible wrinkling modes of the membrane subjected to its actual boundary conditions and loading. The eigenvectors of the tangent stiffness matrix obtained are possible wrinkling shapes of the structure. Then, mode shapes are introduced as initial geometric imperfections in the structure before performing the post-buckling calculations. The amplitude of the initial imperfection introduced at the beginning of the simulation is set to 12.5% of the thickness of the studied membrane. This is the standard imperfection value proposed in Wong and Pellegrino (2006b).

In this study, the numerical scheme is composed of four steps. The first step consists in pre-tensioning the membrane by applying an initial tension to its four edges. This load is due to the counterweights used to position the test specimen. The obtained stress state is considered as an initial stress. In the second step, the compressive displacement $\delta_1$ is applied to the two vertical edges along the $X$-axis. The two horizontal edges are assumed to be fully constrained. Step II is divided into two sub steps. First, an eigenvalue analysis is performed with the imposed displacement $\delta_1$. Then the selected buckling modes are introduced in the model before analyzing the post-buckling response. the method described above was used again in step III. The two vertical edges are fully constrained and a 3 mm displacement $\delta_2$ is imposed on the horizontal edges along the $Y$-axis. Here the eigenvalue analysis is carried out to possibly introduce the new buckling modes which can occur when the tensile load is applied. Then, in step IV the convergence of the numerical simulation is examined, and the wrinkle shape analysis is performed. The flowchart of the simulation procedure is shown in Fig. 26.

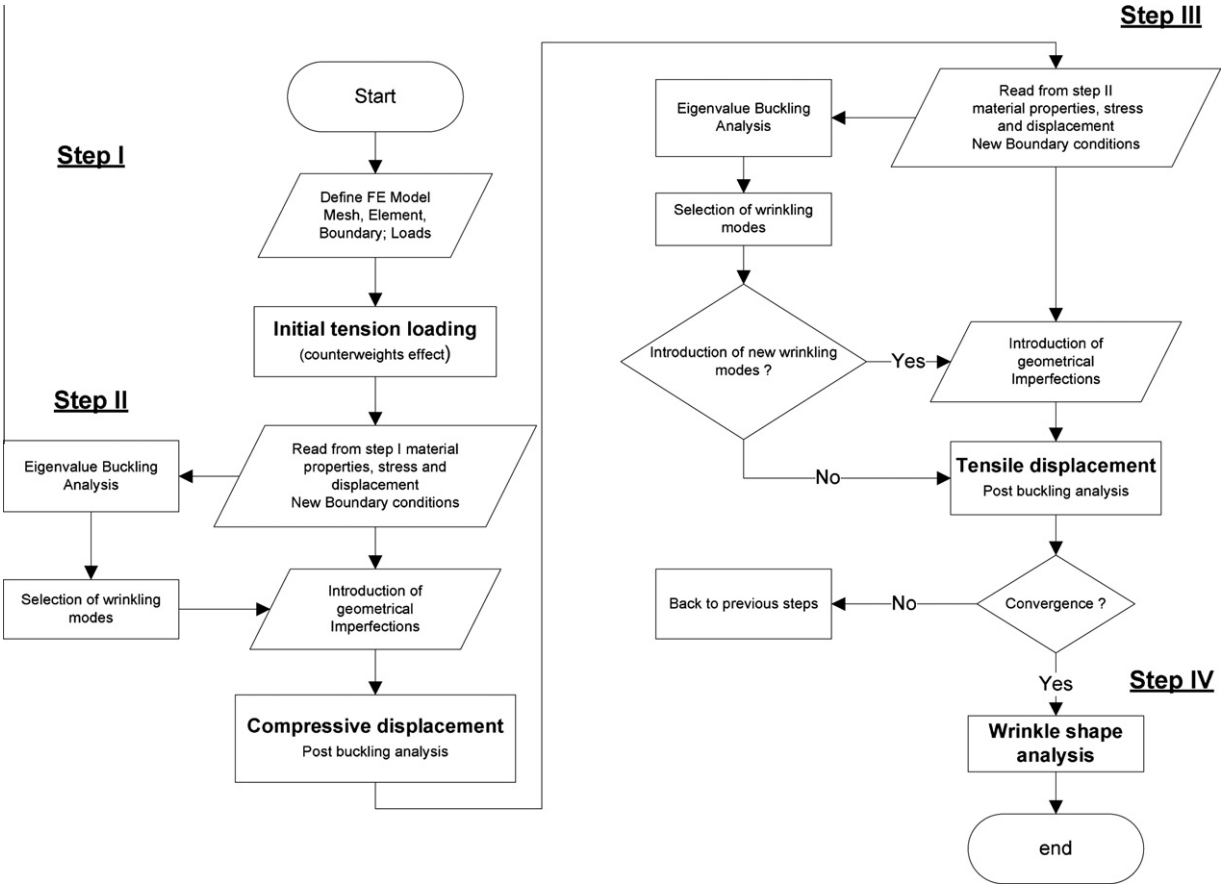


**Fig. 26.** Flowchart of the wrinkling simulation procedure.

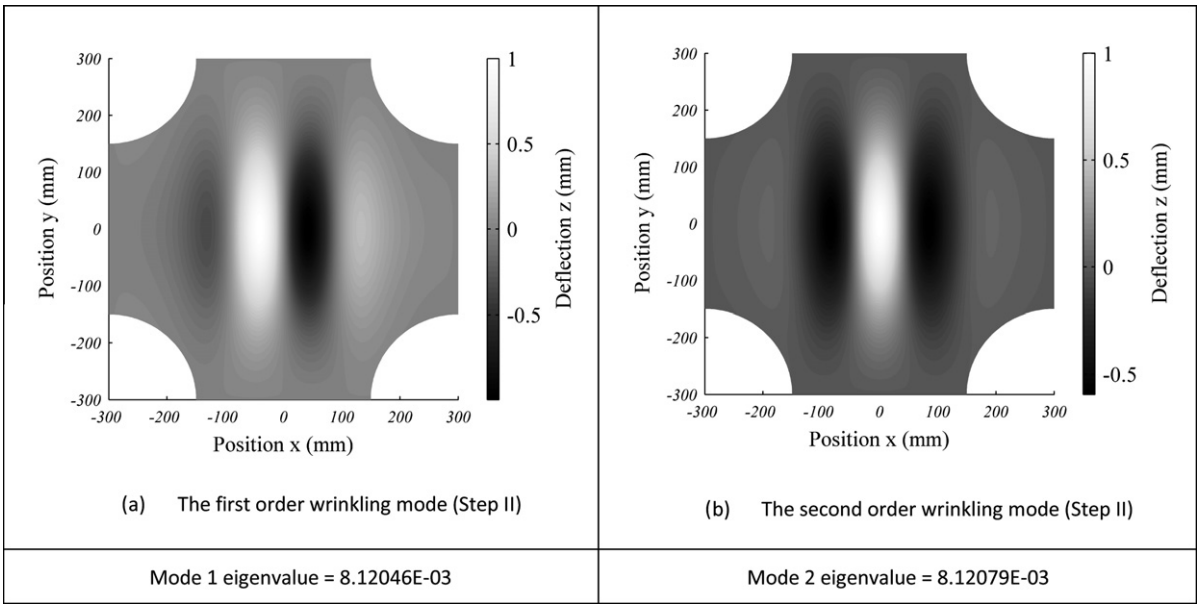


**Fig. 27.** First and second wrinkling modes in step II for $\delta_1 = -2$ mm and $\delta_2 = 0$ mm (specimen thickness 125 μm).

*6.3. Comparison of the wrinkling calculation with the experimental results*

As mentioned earlier, different wrinkle patterns sometimes occurred although the same tensile load was applied on two identical specimens. These different wrinkle shapes match different buckling modes that can be predicted using numerical analysis. To justify this statement, some of the wrinkle patterns observed on the 125 μm test specimens were reproduced using the wrinkling simulation procedure. Different imperfections corresponding to different buckling modes were introduced in the model to obtain the solution issued from a given branch of stability. Fig. 27

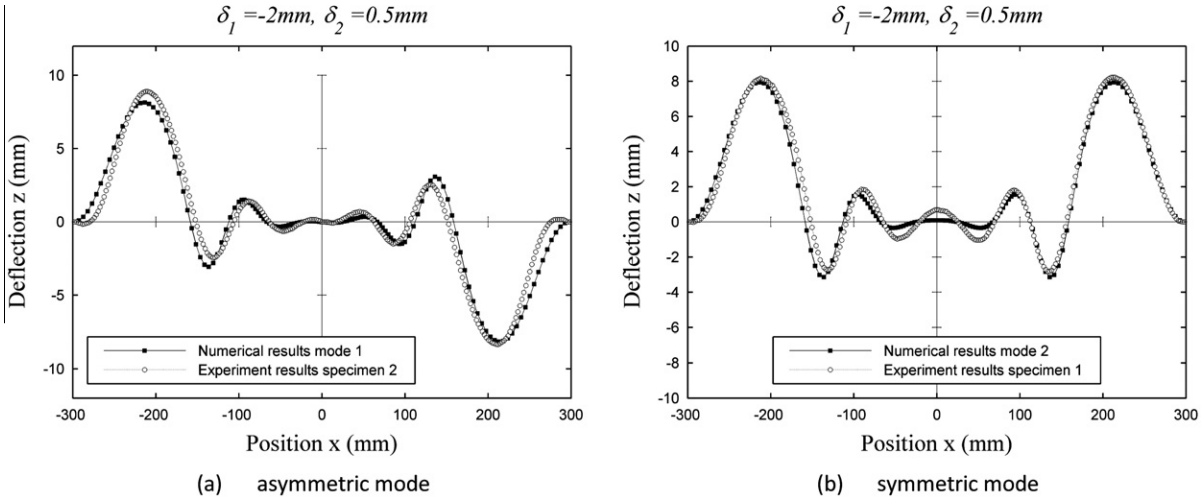


| | Force in the horizontal cross bars (N) | Force in the vertical cross bars (N) |
|---|---|---|
| Load cells | 231.7 | – |
| Numerical results | Mode 1: 233.838 | Mode 1: 0.24 |
| | Mode 2: 233.756 | Mode 2: 0.24 |

**Fig. 28.** Comparison of the numerical and experimental wrinkling results for $\delta_1 = -2$ mm and $\delta_2 = 0.5$ mm (specimen thickness 125 μm).

shows the first two wrinkling modes that are obtained when the compressive displacement $\delta_1$ is set to $-2$ mm. The first wrinkling mode is asymmetric, whereas the second is symmetric. The introduction of one of these modes in our model gives the results presented in Fig. 28 with $\delta_2 = 0.5$ mm and in Fig. 29 with $\delta_2 = 3$ mm. As it has been shown, the numerical and experimental results are very close. Because of the very small thickness of the tested specimens, the eigenvalues corresponding to the first two wrinkling modes are very close. That is the reason why the two modes have been observed throughout the experiment. Nevertheless, the asymmetric mode for $\delta_2 = 0.5$ mm has been watched fifteen times against only three times for the symmetric one. It seems that the first wrinkling mode occurs more often than the second. This trend is not so manifest for the 50 μm test specimens. Indeed, the asymmetric mode was observed twelve times, against six for the symmetric one. For the 25 μm test specimen, it is hard to identify a precise mode, because of the very small bending stiffness of the tested specimens.

The final wrinkle shape does not only depend on the initial bifurcation associated with the first or the second wrinkling modes. Other bifurcations can occur during the loading. They were observed during the experiment when the tensile displacement was applied. Here is a sample of wrinkle evolution for two test specimens when load case two was applied ($\delta_1 = -1$ mm and $\delta_2 = 0$–3 mm. For the tensile displacement $\delta_2 = 0.5$ mm (see Fig. 31) the two test specimens present a wrinkle pattern associated with the first wrinkling mode. Then, during the application of the tensile displacement, a bifurcation occurs on test specimen one and the initially asymmetric wrinkle pat-

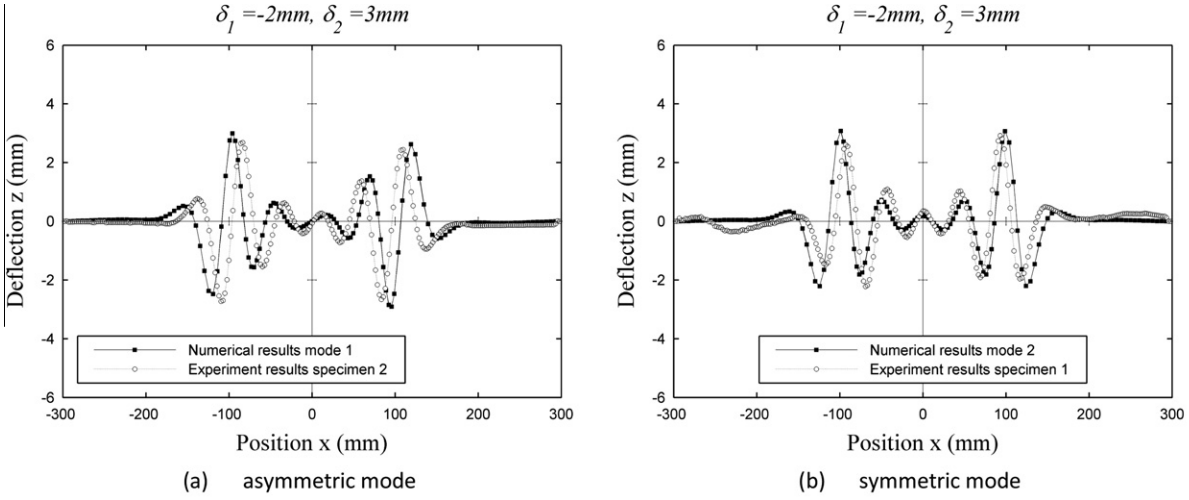


| | Force in the horizontal cross bars (N) | Force in the vertical cross bars (N) |
|---|---|---|
| Load cells | 1503.0 | 45.9 |
| Numerical results | Mode 1: 1474.63 | Mode 1: 58.91 |
| | Mode 2: 1474.62 | Mode 2: 58.85 |

**Fig. 29.** Comparison of the numerical and experimental wrinkling results for $\delta_1 = -2$ mm and $\delta_2 = 3$ mm (specimen thickness 125 μm).

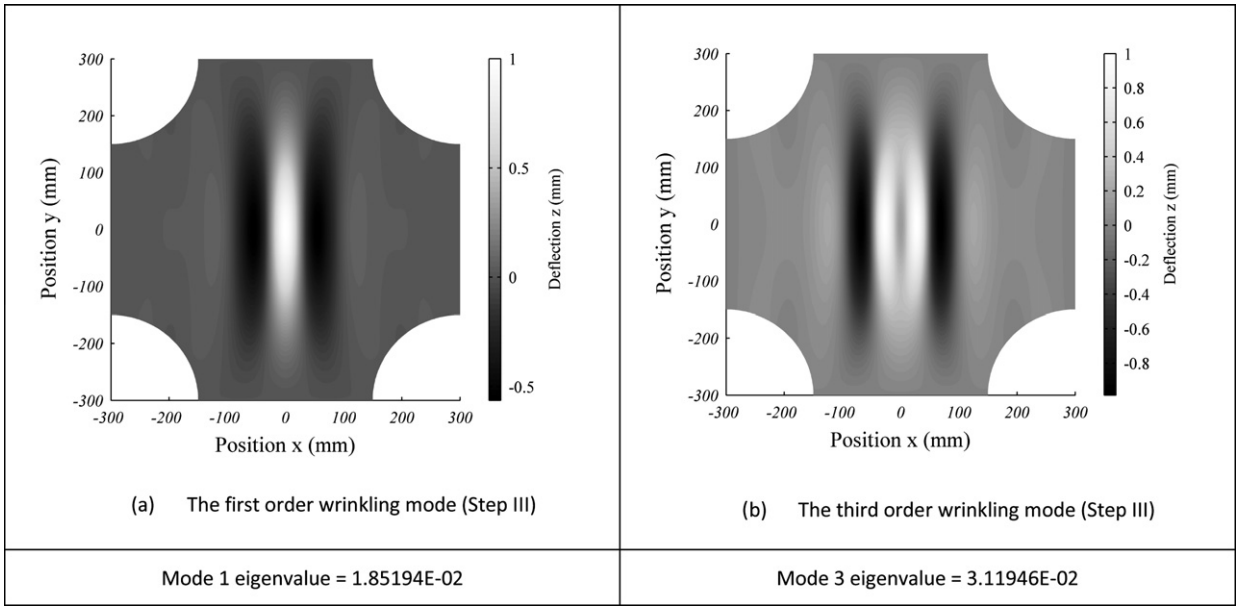


**Fig. 30.** First and third wrinkling modes in step III for $\delta_1 = -1$ mm and $\delta_2 = 3$ mm (specimen thickness 125 μm).

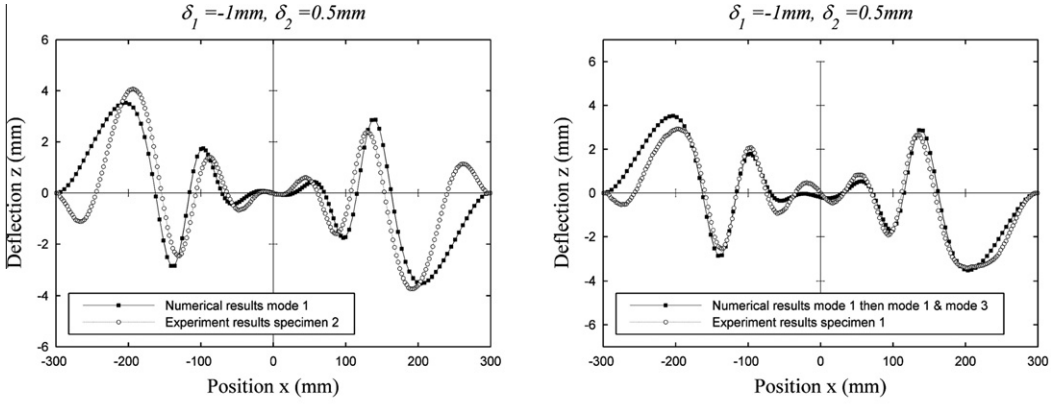


| | Force in the horizontal cross bars (N) | Force in the vertical cross bars (N) |
|---|---|---|
| Load cells | 238.6 | – |
| Numerical results | Mode 1: 236.42 | Mode 1: 0.84 |
| | Mode 1 then mode 1 & 3: 236.42 | Mode 1 then mode 1 & 3: 0.86 |

**Fig. 31.** Comparison of the numerical and experimental wrinkling results for $\delta_1 = -1$ mm and $\delta_2 = 0.5$ mm (specimen thickness 125 μm).

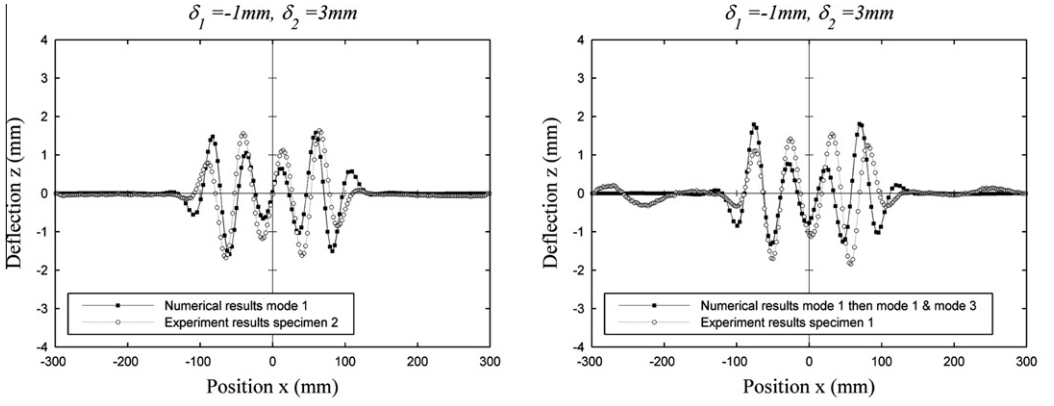


| | Force in the horizontal cross bars (N) | Force in the vertical cross bars (N) |
|---|---|---|
| Load cells | 1560.2 | 122.2 |
| Numerical results | Mode 1: 1538.2 | Mode 1: 132.74 |
| | Mode 1 then mode 1 & 3: 1538.2 | Mode 1 then mode 1 & 3: 132.69 |

**Fig. 32.** Comparison of the numerical and experimental wrinkling results for $\delta_1 = -1$ mm and $\delta_2 = 3$ mm (specimen thickness 125 μm).

tern becomes symmetric when $\delta_2$ = 3 mm (see Fig. 32). For test specimen two, this experimental result was reproduced by the introducing the first wrinkling mode at the beginning of step II (see Fig. 27) and then the new first and third buckling modes at the beginning of step III (see Fig. 30).

Numerical results presented here show that the different kinematic configurations observed during the experiment are issued from different branches of bifurcation. The procedures of wrinkling simulations are now able to reproduce a particular geometry of wrinkle. Nevertheless, the physical problem of wrinkling in thin structures is extremely unstable and unpredictable.

The prediction of bifurcation modes is based on the detection of zero modal stiffness on loading path. When the structure presents several modal stiffnesses very close to zero, a bifurcation can occur according to the lowest mode. The switch to a stable branch associated with a higher mode is also possible. The numerical study has clearly demonstrated this possibility in the case of this study. Indeed, it has been shown that it is possible to choose a desired bifurcation branch by introducing its eigenmode in the solution vector as a geometric imperfection initiating the mode.

From an experimental viewpoint, there is an indetermination about the modes that occur because of an uncertainty on the boundary conditions. Although this uncertainty is reduced to very low values, it stills sufficient to lead up the higher bifurcation modes. This is mainly due to the proximity of branching modes as shown by the eigenvalues of modes 1 and 2 (see Fig. 27). However, we found experimentally that the first mode occurs more frequently than the second mode.

## 7. Conclusions

This paper presents a set of experiments carried out on cruciform specimens. In each experiment, the whole 3D shape of the membrane has been digitized using the fringe analysis method. Detailed results such as the shape, the amplitude and the wavelength of wrinkles are summarized here. Unlike the previous work, the effective realization of this experiment was performed using three study parameters: two kinematic parameters and the thickness of the test specimens. The particular purpose of this work is to observe the reproducibility of the wrinkle patterns that form on the surface of different specimens under nominally identical boundary conditions. A finite element procedure using post-buckling analysis has been used to reproduce some of the wrinkle patterns observed during the experiment and to discuss the uncertainty of the wrinkle shape.

**Table A.7**
Experimental measurement of loads applied to the specimens[a].

| Loading cases | | Specimen thickness 125 μm | | Specimen thickness 50 μm | | Specimen thickness 25 μm | |
|---|---|---|---|---|---|---|---|
| $\delta_1$ (mm) | $\delta_2$ (mm) | *X* axis loading (N) | *Y* axis loading (N) | *X* axis loading (N) | *Y* axis loading (N) | *X* axis loading (N) | *Y* axis loading (N) |
| 0 | 0 | 0 | 0 | 0 | 0 | 0 | 0 |
| 0 | 0.5 | 51.7 | 320.7 | 21.5 | 140.3 | 9.5 | 62.3 |
| 0 | 1 | 119.9 | 624.5 | 55.3 | 275.0 | 24.8 | 122.4 |
| 0 | 1.5 | 191.0 | 917.0 | 88.1 | 397.5 | 40.6 | 179.6 |
| 0 | 2 | 265.6 | 1207.8 | 120.9 | 513.0 | 55.5 | 232.8 |
| 0 | 2.5 | 331.4 | 1453.6 | 149.5 | 608.9 | 69.5 | 279.5 |
| 0 | 3 | 390.1 | 1660.2 | 175.7 | 693.9 | 83.5 | 324.3 |
| −0.5 | 0.5 | | 237.4 | | 112.2 | | 45.3 |
| −0.5 | 1 | 14.1 | 528.3 | | 234.8 | | 99.9 |
| −0.5 | 1.5 | 51.5 | 812.9 | 22.5 | 356.2 | | 155.2 |
| −0.5 | 2 | 101.9 | 1108.8 | 44.1 | 470.9 | 14.8 | 209.7 |
| −0.5 | 2.5 | 154.1 | 1360.7 | 67.3 | 577.9 | 25.8 | 259.1 |
| −0.5 | 3 | 207.8 | 1597.1 | 91.5 | 674.0 | 37.5 | 308.0 |
| −1 | 0.5 | | 238.6 | | 110.1 | | 26.8 |
| −1 | 1 | | 507.7 | | 224.9 | | 96.9 |
| −1 | 1.5 | 15.7 | 778.9 | | 340.7 | | 150.4 |
| −1 | 2 | 45.8 | 1062.4 | 17.2 | 453.6 | 5.9 | 203.1 |
| −1 | 2.5 | 81.6 | 1321.6 | 32.3 | 556.2 | 13.3 | 246.2 |
| −1 | 3 | 122.2 | 1560.2 | 50.1 | 657.8 | 21.8 | 300.6 |
| −1.5 | 0.5 | | 233.1 | | 72.2 | | 41.6 |
| −1.5 | 1 | | 492.9 | | 214.6 | | 91.1 |
| −1.5 | 1.5 | | 756.0 | | 328.6 | | 143.0 |
| −1.5 | 2 | 20.1 | 1036.0 | | 439.2 | | 192.0 |
| −1.5 | 2.5 | 44.6 | 1285.5 | 14.3 | 540.8 | 7.3 | 241.9 |
| −1.5 | 3 | 74.5 | 1524.7 | 27.9 | 638.3 | 14.2 | 291.1 |
| −2 | 0.5 | | 231.7 | | 99.2 | | 40.8 |
| −2 | 1 | | 488.5 | | 208.7 | | 89.4 |
| −2 | 1.5 | | 743.1 | | 317.9 | | 138.2 |
| −2 | 2 | | 1017.0 | | 428.8 | | 190.9 |
| −2 | 2.5 | 23.4 | 1262.6 | 5.2 | 527.6 | | 238.4 |
| −2 | 3 | 45.9 | 1503.3 | 15.5 | 629.9 | 7.1 | 286.2 |
| −2.5 | 0.5 | | 224.8 | | 97.1 | | 41.1 |
| −2.5 | 1 | | 479.4 | | 206.9 | | 89.2 |
| −2.5 | 1.5 | | 732.7 | | 315.0 | | 138.7 |
| −2.5 | 2 | | 993.7 | | 421.3 | | 187.9 |
| −2.5 | 2.5 | 9.6 | 1235.3 | | 520.7 | | 234.8 |
| −2.5 | 3 | 26.2 | 1469.1 | 10.4 | 619.5 | | 282.0 |
| −3 | 0.5 | | 215.2 | | 95.0 | | 37.8 |
| −3 | 1 | | 472.7 | | 200.7 | | 85.9 |
| −3 | 1.5 | | 721.6 | | 308.9 | | 134.1 |
| −3 | 2 | | 980.6 | | 416.8 | | 184.3 |
| −3 | 2.5 | | 1221.4 | | 513.1 | | 232.2 |
| −3 | 3 | 16.5 | 1441.3 | 5.3 | 613.4 | | 278.1 |

[a] Results presented here are the averages of the data recoded for the three test specimens. Empty cells correspond to non-significative value – i.e. less than the 5N of the measured friction.

From the experiment and the simulations, the following conclusions can be stated:

- A mechanism of wrinkle division has been observed during the experiment. The creation of a new wrinkle has been explained as a local mode change or a local buckling of an existing wrinkle.
- Non-unique wrinkle shapes have been observed over repeated experiments. The comparison with the numerical analysis showed that the different shapes of wrinkling experimentally observed match the numerical predictions issued of different branches of bifurcation.

## Acknowledgments

Financial support from CNES and EADS Astrium is gratefully acknowledged. The author thank S. Kervision and C. Lemaire for useful corrections.

## Appendix A

See Table A.7.

## References

Balmforth, N.J., Craster, R.V., Slim, A.C., 2008. On the buckling of elastic plates. Quarterly Journal of Mechanics and Applied Mathematics 61 (2), 267–289. URL <http://qjmam.oxfordjournals.org/cgi/content/abstract/61/2/267> .

Blandino, J., Jonhston, J., Miles, J., Soplop, J., 2001. Thin film membrane wrinkling due to mechanical and thermal loads. In: 42th AIAA/ASME/ASCE/AHS/ASC Structures, Structural Dynamics and Material Conference and Exhibit.

Blandino, J., Jonhston, J., Miles, J., Dharamsi, U., 2002a. The effect of asymmetric mechanical loading on membrane wrinkling. In: 43th AIAA/ASME/ASCE/AHS/ASC Structures, Structural Dynamics and Material Conference and Exhibit.

Blandino, J.R., Johnston, J.D., Dharasi, U.K., 2002b. Corner wrinkling of a square membrane due to symmetric mechanical loads. Journal of Spacecraft and Rockets 39 (5), 717–724.

Cerda, E., Ravi-Chander, K., Mahadevan, L., 2002. Thin films: winkling of an elastic sheet under tension. Nature 419, 579–580. URL <http://dx.doi.org/10.1038/419579b> .

Crisfield, M., 1997. Non-Linear Finite Element Analysis of Solids and Structures: Advanced Topics. John Wiley & Sons, Inc., New York, NY, USA.

DuPont, 2006. Dupont kapton vn polyimide film technical data sheet. Tech. rep., DuPont.

Epstein, M., Forcinito, M.A., 2001. Anisotropic membrane wrinkling: theory and analysis. International Journal of Solids and Structures 38 (30–31), 5253–5272.

Holo3, December 2006. Logiciel FAF FringeAnalysis. Holo3.

Jenkins, C., 2001. Gossamer Spacecraft: Membrane and Inflatable Structures Technology for Space Applications. AIAA.

Jenkins, C., Haugen, F., Spicher, W., 1998. Experimental measurement of wrinkling in membranes undergoing planar deformation. Experimental Mechanics 38, 147–152.

Kang, S., Im, S., 1997. Finite element analysis of wrinkling membranes. Journal of Applied Mechanics 64, 263–269.

Mansfield, E.H., 1968. Tension field theory: a new approach which shows its duality with inextensional theory. In: XII Int. Cong. Appl. Mech., pp. 305–320.

Mansfield, E.H., 1970. Load transfer via a wrinkled membrane. In: Proceeding of the Royal Society.

Mikulas, M.M., 1964. Behavior of a flat stretched membrane wrinkled by the rotation of an attached hub. Tech. rep. D-2456, NASA.

Miyamura, T., 2000. Wrinkling on stretched circular membrane under in-plane torsion: bifurcation analyses and experiments. Engineering Structures 22 (11), 1407–1425.

Pipkin, A., 1986. The relaxed energy density for isotropic elastic membranes. IMA Journal of Applied Mathematics 36, 8599.

Riks, E., 1979. An incremental approach to the solution of snapping and buckling problems. International Journal of Solids and Structures 15 (7), 529–551.

Robinson, D.W., Reid, G., 1993. Interferogram Analysis Digital Fringe Pattern Measurement Techniques. Institute of Physics Publishing.

Stein, M., 1959. Loads and deformation of buckled rectangular plates. Tech. rep. R40. National Aeronautics and Space Administration.

Stein, M., Hedgepeth, J., 1961. Analysis of partly wrinkled membranes. Tech. rep. D-813, NASA.

Surrel, J., Surrel, Y., 1998. La technique de projection de franges pour la saisie des formes d'objets biologiques vivants. Journal of Optics 29 (1), 6–13.

Wagner, H., 1929. Flat sheet metal girders with very thin metal web. Tech. rep. 604, National Advisory Committee for Aeronautics.

Wang, C., Du, X., Tan, H., He, X., 2009. A new computational method for wrinkling analysis of Gossamer space structures. International Journal of Solids and Structures 46 (6), 1516–1526.

Wong, Y., Pellegrino, S., 2006a. Wrinkled membranes part I: experiments. Journal of Mechanics of Materials and Structures 1, 1–23.

Wong, Y., Pellegrino, S., 2006b. Wrinkled membranes part III: numerical simulations. Journal of Mechanics of Materials and Structures 1, 61–93.

Yoshizawa, T., 2009. Handbook of Optical Metrology: Principles and Applications. CRC Press.

Zhang, Z., Zhang, D., Peng, X., 2004. Performance analysis of a 3d full-field sensor based on fringe projection. Optics and Lasers in Engineering 42 (3), 341–353.